

Experimental and simulation results of two-dimensional prototype anti-scatter grids for mammography

Cha-Mei Tang^a, Tom Fewell^b, Robert Jennings^b,
Rebecca Fahrig^c, David Jaffray^d, Martin Yaffe^e

^aCMT, Creatv MicroTech, Inc, Potomac MD 20854

^bCenter for Devices and Radiological Health,
Food and Drug Administration, Rockville, MD 20857

^cStanford University, Stanford, CA 94305

^dOakland University, Rochester, MI 48309-4401

^eUniversity of Toronto, Toronto, Ontario M4N4M5 Canada

ABSTRACT

Experimental and simulation results are reported here for two-dimensional, air-core, anti-scatter grids designed for mammography. Two unfocused nickel grids, 2 cm² in size, were fabricated. Monte Carlo simulations were performed using a Mo-anode spectrum source and added Mo filtration. Preliminary calculations for a 2 mm-high nickel grid and a 4 cm Lucite phantom indicate that a scatter-to-primary ratio below 3% can be achieved even 3 cm from the center of the grid. Experiments to test the performance of the grids have been conducted at the FDA using a Mo target, a Mo filter, and a Lucite phantom, with a germanium detector. These nickel grids increase transmission of the primary x-rays and reduce transmission of the x-rays in the scattered directions compared to a conventional one-dimensional grid (a mammographic grid made by Smit Röntgen). Thus, two-dimensional nickel grids have the benefit of producing smaller scatter-to-primary ratio than a conventional reference grid, and improving contrast. The demonstration of larger focused grids is the next goal.

1. INTRODUCTION

Most commercially available mammographic anti-scatter grids are one-dimensional, focused arrays of lead lamellae, sandwiched between more x-ray transparent spacer materials such as fiber or wood.¹⁻¹² Two-dimensional (2D), air-core, focused, anti-scatter grids are expected to be able to significantly reduce scatter-to-primary ratio and increase primary transmission in mammography.

In this paper, we report experimental and simulation results for two prototype 2D, air-core anti-scatter grids. The fabrication method uses x-ray lithography and electroplating, which allows the fabrication of high aspect ratio metal parts.¹³⁻¹⁶ The grids are made of nickel (Ni) with 20 μm thick walls (lamella) and 300 μm period. This geometry provides an 87.1% transmission of primary radiation. Grids of a desired grid ratio are obtained by stacking an appropriate number of layers, each approximately 250-350 μm thick.¹⁶

The first prototype (Ni.1) is 1.48 cm x 1.48 cm and the second prototype (Ni.2) is 1.32 cm x 1.44 cm. Each layer of the grid is assembled from nine smaller grid pieces. Figure 1 shows the simplified drawing of the parts of the Ni.2 grid before assembly. The assembly technique allows construction of large grids.¹⁶

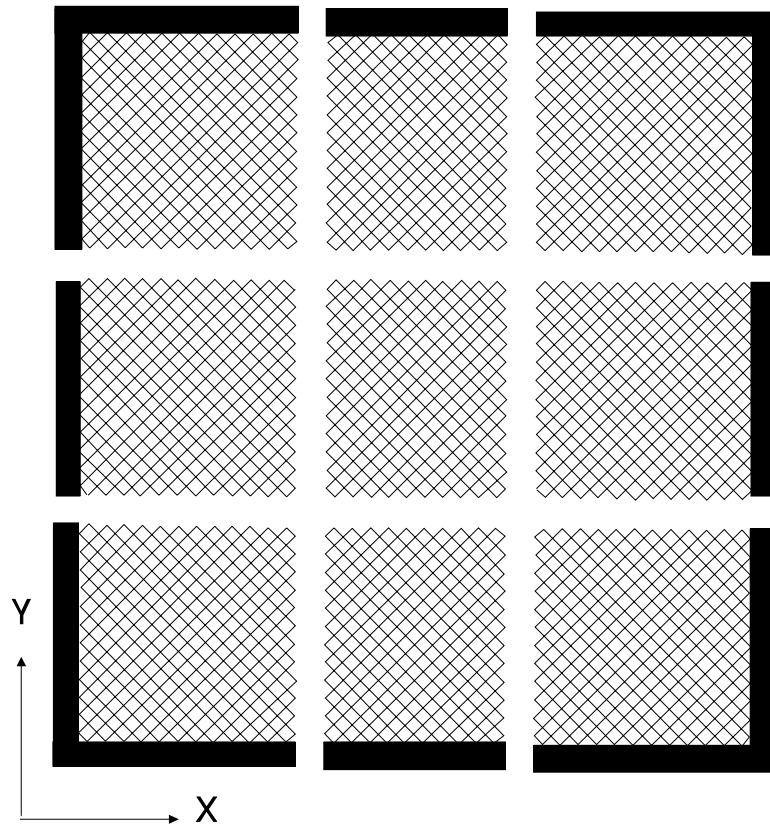


Fig. 1. The parts of Ni.2 grid before assembly.

2. MONTE-CARLO SIMULATION OF Ni ANTI-SCATTER GRID AT MAMMOGRAPHIC ENERGIES

The typical approach to the calculation of scatter-to-primary ratios (S/P) uses a Monte Carlo simulation to calculate the outcome of several thousand photon histories, where a new calculation must be performed for each acquisition geometry and for each grid that is being tested. In order to simplify the process (and to avoid lengthy and repetitious calculations), we combined a Monte Carlo calculation of scatter fields with a deterministic model of the interaction of the x-ray photons with the anti-scatter grid. Although both stages of the model include certain simplifications, estimates of appropriate grid design parameters can be derived from the model.

2.1 Monte Carlo Simulation Model

The geometry modeled in the Monte Carlo simulations is shown in Fig. 2. The fan beam originates at a point focus, and covers a 20 cm x 20 cm cross-sectional area. The x-ray source, one edge of the phantom, and one edge of the detector area are aligned at the chest wall; since no chest-equivalent material was included in the simulation, a small underestimate of scatter close to the chest wall was assumed. Note that the source-to-detector distance was held constant at 60 cm for all phantom thicknesses.

The breast was modeled by a homogeneous block of Lucite, with a cross-sectional area of 20 cm x 20 cm, of variable thickness T . Although an area of 400 cm² is rather large for a breast (typical values for compressed breast area range from 35 cm² to 270 cm², with radii of 4.7 cm and 12.7 cm respectively for a hemi-cylindrical geometry), this model allows examination of S/P for a range of breast sizes. Note that the typical drop in S/P generally seen at the edges of the breast will not be present in the scatter field. Previous investigators have shown that a 4 cm thick block of Lucite results in the same amount of radiographic attenuation as 5 cm of BR-12 (a common breast-equivalent phantom material).¹⁷ Scatter fields were therefore calculated for Lucite thicknesses of 2, 4, and 6 cm, which should represent roughly 3, 5, and 7 cm of breast tissue, respectively. Jing et.al. (1998) have also argued that the angular distribution of scatter generated in Lucite is likely to be similar to that of breast tissue and of BR-12.¹⁸

A 30 kVp spectrum with 30 μ m of added Mo filtration, taken from the measured data of Fewell and Shuping (1978), was used for all of the calculations presented here. The average photon energy of the spectrum is 18.4 keV, slightly higher (\sim 1.5 keV) than current tubes that have a beryllium window instead of a glass window. For spectra with the same added filtration but at energies of 25 and 35 kVp, the mean energy changed very little - from 17.7 to 19.4 keV. In previous studies of S/P for scanning slot geometries, it had been shown that this change in energy can lead to changes in S/P on the order of \sim 10%.¹⁹

The Monte Carlo simulation was implemented using the EGS4 code system,²⁰ including the atomic binding effect on Compton scattering²¹ and the effect of molecular structure of

the Lucite on coherent scatter.²² Note that this code has been compared with previously published experimental data,¹⁷ and has been shown to agree within 10% for Lucite thicknesses up to 6 cm. Each run traced the histories of 100,000 photons. Typical data generated by the Monte Carlo simulation are presented in Table I. The parameters of each photon were recorded at the point when the photon crosses the 'detector' or grid plane. The first column indicates whether the photon had undergone a scatter event or not, where 1 indicates a primary unscattered photon, 2 indicates a photon whose only interactions were coherent scatter, and 3 indicates a photon that had undergone incoherent scatter. The second column indicates the energy of the photon at the time of recording. The third, fourth and fifth columns indicate the location of the photon in 3-D space, and the last three columns are the directional cosines of the photon trajectory (i.e. the cosines of the angles that the photon trajectory makes with the x-, y- and z-axes).

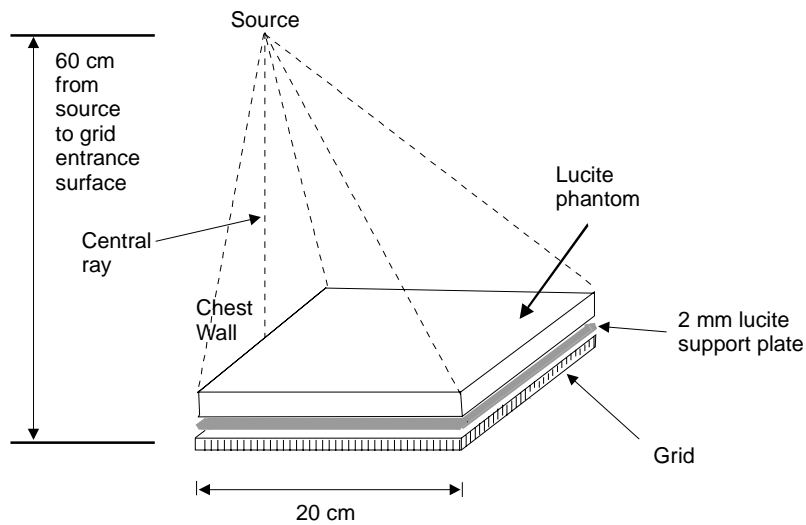


Fig. 2. Geometry modeled in the Monte Carlo simulation.

Table 1. Sample data (5 histories) produced by the EGS4 Monte Carlo simulation code.

Interaction Label	Energy (keV)	Location X	Location Y	Location Z	Dir. Cos. X	Dir. Cos. Y	Dir. Cos. Z
2	15	15.34	-5.09	60.00	-0.125	0.483	0.867
1	18	12.44	-2.03	60.00	0.209	-0.033	0.979
1	18	0.21	-6.31	60.00	0.003	-0.105	0.994
2	16	16.41	-3.82	60.00	-0.212	0.908	0.359
3	8	10.80	5.07	60.00	0.122	0.382	0.916

2.2 Deterministic Model

The upper surface of the grid is assumed to lie 60 cm from the source, and covers the full 20 cm x 20 cm area of the phantom and field. This area is then divided into grid elements,

according to the grid geometries (A) 20 μm thick lamella and 300 μm period and (B) 10 μm thick lamella and 150 μm period. A schematic diagram of the result is shown in Fig. 3.

The following calculations were performed for each photon history:

1. The grid element $(u,v)_{\text{in}}$ that the x-ray photon hits at the grid entrance surface was determined using the (x,y,z) specified in the history file.
2. The grid element $(u,v)_{\text{out}}$ that the x-ray photon hit at the grid exit surface was determined, using the $(x,y,z)_{\text{in}}$ location of the photon, the angle cosines and the height of the grid.
3. The number of lamellae crossed in the x and y directions was determined by subtracting $(u,v)_{\text{in}}$ from $(u,v)_{\text{out}}$.
4. When $[(u,v)_{\text{out}} - (u,v)_{\text{in}}]$ was not equal to 0, the path length through a grid lamella, in the x- and/or y-directions, was calculated, and the fractional probability of the photon reaching $(u,v)_{\text{out}}$ was determined as follows

$$P_{\text{out}} = 1.0 \times e^{[-\mu(\Delta x|u_{\text{out}} - u_{\text{in}}| + \Delta y|v_{\text{out}} - v_{\text{in}}|)]}$$

where μ is the attenuation coefficient of Ni at the energy of the photon, and Δx and Δy are the path lengths of the photon through the lamellae in the x and y directions respectively.

Using the interaction label, the numbers of primary, coherent and incoherently scattered photons reaching the exit plane of each grid element were determined by summing up the results of steps 1 to 4. Note that the final number of photons in a grid element can be non-integer, due to the effect of the grid attenuation. The field was then divided into 20 equally spaced radial segments, and mean values for S/P and for primary transmission were calculated as a function of radial distance from the central ray at the chest wall. The S/P was calculated from photon statistics alone, and was not weighted in any way to account for the interaction of the photons with the detector. The alternate approach of energy-weighting the photons prior to summation led to differences in S/P on the order of ~5%. This model assumes that all interactions in the grid were photoelectric in nature, and that no additional scatter occurred in the grid.

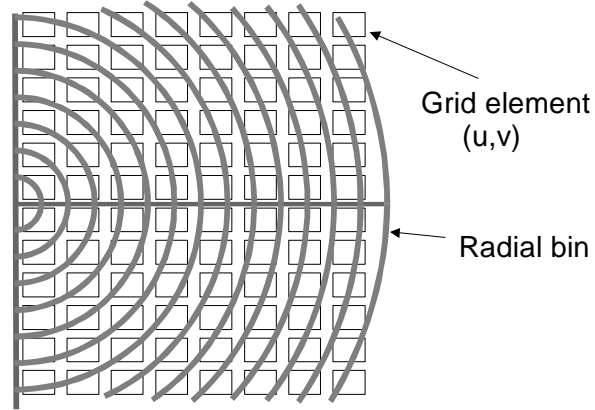


Fig. 3. Schematic representation of the grid geometry, including evenly spaced radial bins

2.3 Results

The data are plotted as a function of radial distance from the central ray, and as a function of grid height. A few notes regarding the results:

1. The S/P at the input plane of the grid, for the 2, 4, and 6 cm Lucite phantoms were 0.341, 0.663, and 0.989, respectively.
2. The statistics in the first 3 or 4 radial bins are not very reliable, since the area covered by each bin was relatively small. This led to some variability that was due to noise rather than to geometrical effects.

Note that, for an unfocused grid, we were only interested in the S/P within 1-2 cm from the center, since it is not relevant for larger radial distances. Figure 4 is a plot of S/P ratio for 4 cm Lucite, at 30 kVp and grid with 20 μm thick lamella and 300 μm period for a grid height of 1 mm and 2 mm. The increase of S/P for large radial distance is primarily caused by reduction of primary radiation, which in turn is caused by an unfocused grid. In the future, the statistics will be improved with longer runs.

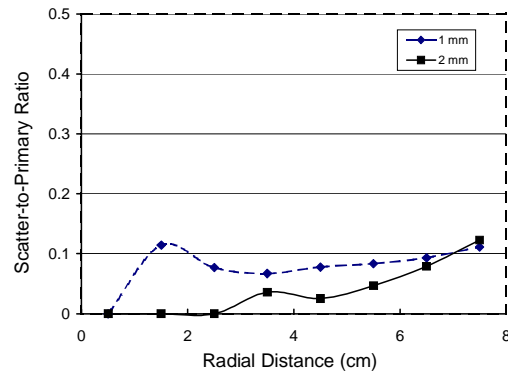


Fig. 4. Scatter-to-primary ratio for 4 cm Lucite, at 30 kVp and grid with 20 μm thick lamella and 300 μm period for a grid height of 1 mm and 2 mm.

3. EXPERIMENTS AT MAMMOGRAPHIC ENERGIES

Experiments to measure the performance of the grid were designed and performed at the Center for Devices and Radiological Health, Food and Drug Administration, Rockville, Maryland. Several experimental options were analyzed. The following procedure was chosen primarily based on the small size and unfocused nature of the grid.

The goal was to measure the transmission of the incident x-ray beam impinging on the grid as a function of its direction. The coordinate system for the measurements is shown in Fig. 5. The angle between the x-ray beam and the normal direction to the grid is ϕ , and the angle, in the plane of the grid, of the structure (lamellae or walls) relative to the axis of rotation is θ . The x-axis of the grid is shown in Fig. 1. The data collected with $\phi=0$, normalized by a measurement with no grid in place, gives the transmission of the primary radiation. The data for $\phi>1^\circ$ gives the transmission of the scattered radiation. Even though direct measurements of the scatter-to-

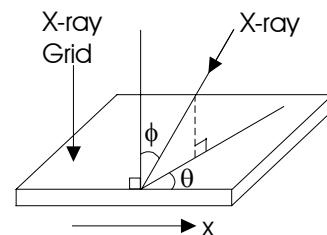


Fig. 5 The geometry for measurement of transmission of radiation.

primary ratio (S/P) could not be obtained experimentally due to the small size of the grid, the experimental procedure described here can provide detailed comparisons of the performance of various grids.

3.1 Experimental Setup and Data Collection Procedure

The experimental setup, shown in Fig. 6, used a narrow x-ray beam and measured the x-ray transmission as a function of the angle of incidence. The x-ray source was a Eureka x-ray tube with a molybdenum (Mo) target and 30 μm Mo filter. The x-ray beam went through a 3.2 mm diameter aperture placed 7 cm from the source, followed immediately by a 4 cm thick polymethyl-methacrylate (PMMA, also called Lucite) phantom. A second 2 mm diameter aperture was placed 81 cm from the x-ray source. A germanium detector was placed 119 cm from the second aperture. A holder for the grid was machined and mounted on a rotation stage. The grid can be manually moved in the vertical direction and in the horizontal direction. The grid was placed 1.3 cm in front of the detector.

The diameter of the detector was 11.3 mm, giving an active area over 100 mm^2 . The x-ray beam diameter at the grid was 5 mm. A 3 mm diameter aperture was placed in front of the detector to pick out the central portion of the x-ray beam after propagating through the grid. The apertures and the source were aligned using x-ray film. The x-ray flux was sufficiently reduced with the small aperture to perform single photon counting to obtain x-ray spectra.

For comparison, measurements were also made with a commercial mammographic grid made by Smit Röntgen. This is a 1D grid made of lead and fiber. The lead lamella thickness is 16 μm and the interspace fiber material thickness is 300 μm (31 strips per cm). The outside surfaces are made of carbon fiber; the grid ratio is 5:1; the focal distance is 60 cm.

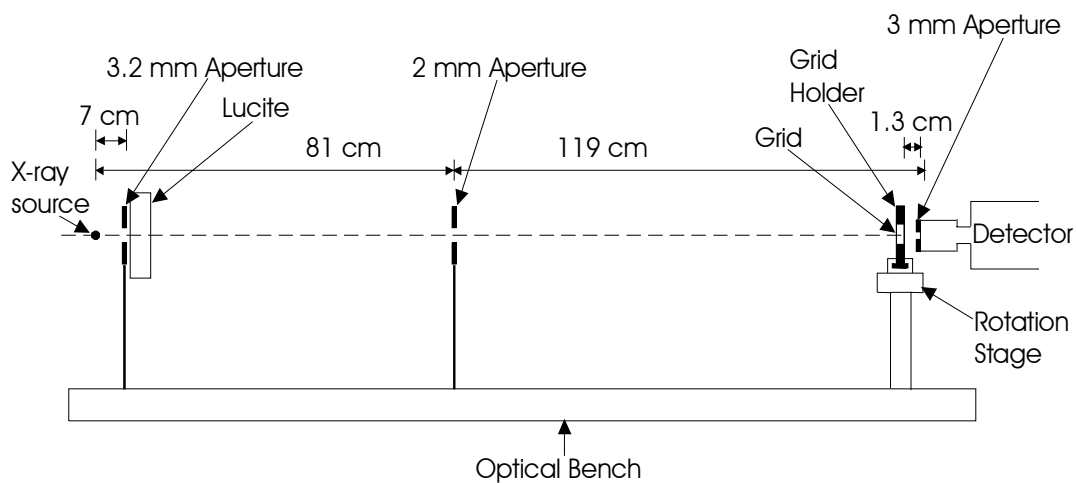


Fig. 6 The experimental setup. (Not drawn to scale.)

The transmission of x-rays as a function of x-ray energy for 20 μm thick nickel and iron, and 16 μm thick lead are plotted in Fig. 7. For energies below 16.5 keV, the transmission of lead is similar to iron. Nickel is a little better than iron for the same thickness. For energies above 16.5 keV, the attenuation of radiation of lead is superior.

The experimental procedure was to align the grid perpendicular to the x-ray beam with the rotating stage set at $\varphi=0^\circ$. When the grid was rotated, the grid walls intercepted more of the x-ray beam. Data were taken for the following angles: $\varphi=0^\circ, \pm 1^\circ, \pm 2^\circ, \pm 4^\circ, \pm 6^\circ, \pm 8^\circ, \pm 10^\circ, \pm 12^\circ, \pm 15^\circ$ and $\pm 20^\circ$. At each angle, an x-ray spectrum was taken. The raw spectra are corrected for Compton scattering and K fluorescence of the Ge to generate the true x-ray spectrum that passed through the grid.

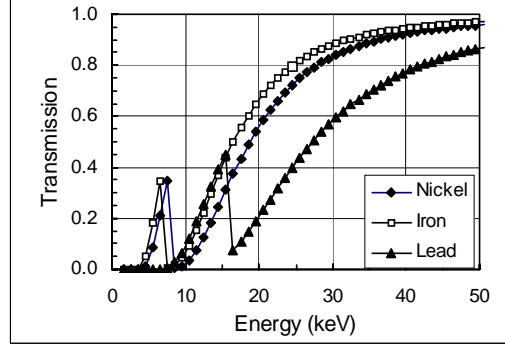


Fig. 7. Transmission of x-ray as a function of the x-ray energy for 20 μm thick nickel and iron, and 16 μm thick lead.

Using the x-ray spectrum, one can predict the effect of the grid on the energy absorbed by a mammography screen.

The screen was assumed to be a Kodak Min-R screen with a phosphor loading of 33.5 mg/cm^2 of $\text{Gd}_2\text{O}_2\text{S}$. Energy absorption data for this screen were calculated based on the paper by Dance et al. 1990. The percentage of transmission $T(\theta, \varphi)$ is obtained using the following formula,

$$T(\theta, \varphi) = \frac{\int_0^{E_{\max}} S(E, \theta, \varphi) A(E) E dE}{\int_0^{E_{\max}} S_0(E) A(E) E dE},$$

where $S(E, \theta, \varphi)$ is the corrected x-ray spectrum, $A(E)$ is the intensifying screen energy absorption function, $S_0(E)$ is the spectrum of the radiation without the grid, E is the x-ray energy, E_{\max} is the kVp of the x-ray tube and T is the x-ray transmission as detected by the screen.

3.2 Data at 30 kVp

Data reported here were taken at 30 kVp and approximately 2.0 mA current using a large focal spot (nominal 0.3 mm) for a 2.00 mm thick Ni grid fabricated with mask layout 1 (Ni.1 grid), and for a 1.78 mm thick Ni grid fabricated with mask layout 2 (Ni.2 grid). A one minute exposure was used at $\varphi=0^\circ$. At larger angles, the exposure time was increased to compensate for the decrease of x-ray transmission.

For $\theta=0^\circ$: The conventional reference grid was positioned so that the lead lamellae are oriented in the vertical direction and the grid was centered. Fig. 8 shows curves of transmission as a function of angle ϕ for the Ni.1, Ni.2 and the conventional reference grids.

- **Transmission of the Primary Radiation ($\phi=0^\circ$):** The transmission of the Ni.2 grid at $\phi=0^\circ$ was 84.8%, very close to the predicted value of 87.1% based on the grid dimensions. The transmission of the Ni.1 grid at $\phi=0^\circ$ was 75.5%, much less than the Ni.2 grid. The transmission of the conventional reference grid at 0° was 71.7% due to the interspace material and carbon fiber covers.
- **Transmission of Scattered Radiation ($\phi > 1^\circ$):** For $\phi > 1^\circ$ the transmission of the Ni.1 grid was lower than that of the Ni.2 grid, consistent with the grid ratio. The slopes of the transmission curves for all three grids are consistent with transmission determined by geometric parameters only, specifically the height of the grid and the periodicity.

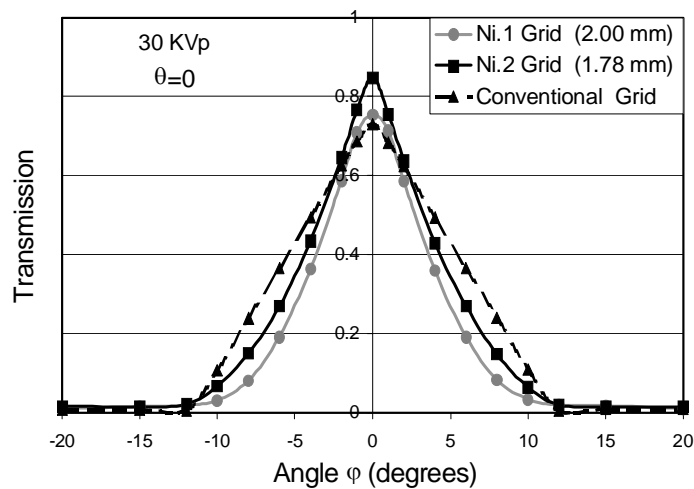


Fig. 8 Transmission of x-rays at 30 kVp as a function of the normal incidence angle ϕ for $\theta = 0^\circ$.

For $\theta=45^\circ$: Fig. 9 shows curves of transmission as a function of the angle ϕ for the Ni.1 and Ni.2 grids. For ϕ between 1° and 10° , the slopes of the transmission for the Ni.1 and Ni.2 grids are consistent with the transmission based on geometry. However, between 10° and 20° the transmission is between 5 to 10 percent. The conventional reference grid curve is calculated based on geometry.

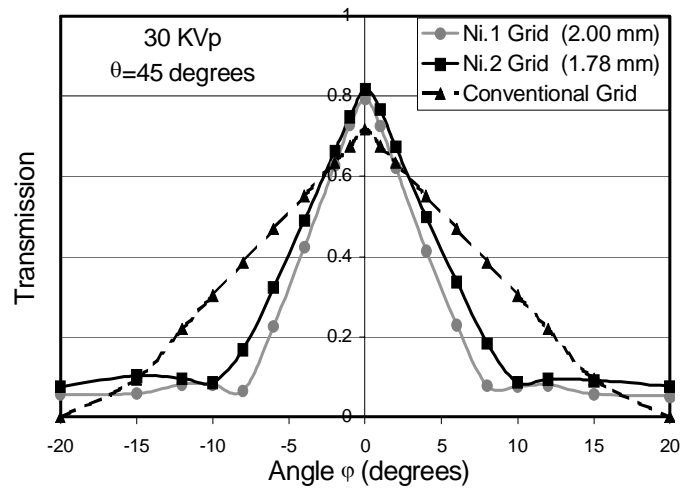


Fig. 9 Transmission of x-rays at 30 kVp as a function of the normal incidence angle φ for $\theta = 45^\circ$.

For $\theta=90^\circ$: The transmissions of the Ni.1 and Ni.2 grids are identical to the transmission curves shown in Fig. 8. For the conventional reference grid, the measured transmission at $\varphi=0^\circ$ is 71.7% and the calculated transmission for angles up to $\varphi=20^\circ$ decreases only slightly, see Fig. 10.

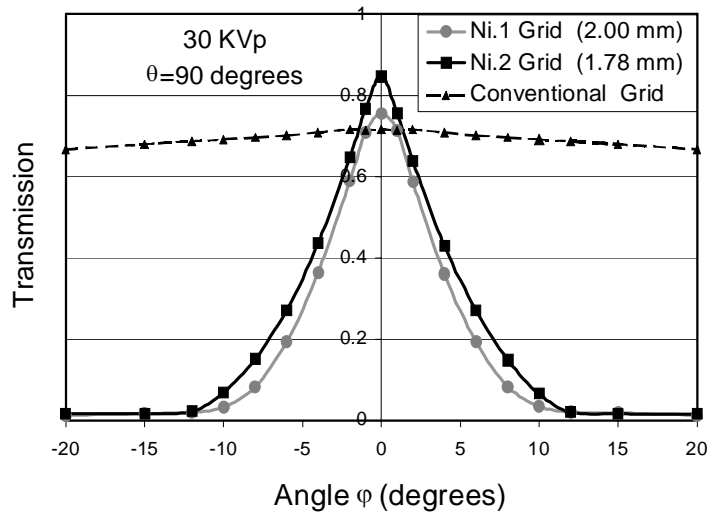


Fig. 10 Transmission of x-rays at 30 kVp as a function of the normal incidence angle φ for $\theta = 90^\circ$.

The shortfall of the observed primary transmission from the predicted primary transmission at $\varphi = 0$ degrees for each grid is due to tilt of the grid in the vertical direction during measurement. The consistently lower transmission of primary transmission of the Ni.1 grid relative to the Ni.2 grid is due to imperfect alignment of the

grid layers during stacking and also due to slight buckling of some grid walls during assembly.

3.3 Data at 26 kVp

Data for the Ni.2 grid was also collected at 26 kVp for $\theta = 0^\circ$ and $\theta = 45^\circ$, shown in Fig. 11. The transmission results are almost identical to that for Ni.2 for $\varphi < 10^\circ$. For $\theta = 0^\circ$, the transmission for 26 kVp is about 0.01 smaller than transmission for 30 kVp. For $\theta = 45^\circ$, the transmission for 26 kVp is about 0.03 smaller than transmission for 30 kVp. This is consistent with the spectrum of the x-ray source and the attenuation of Ni.

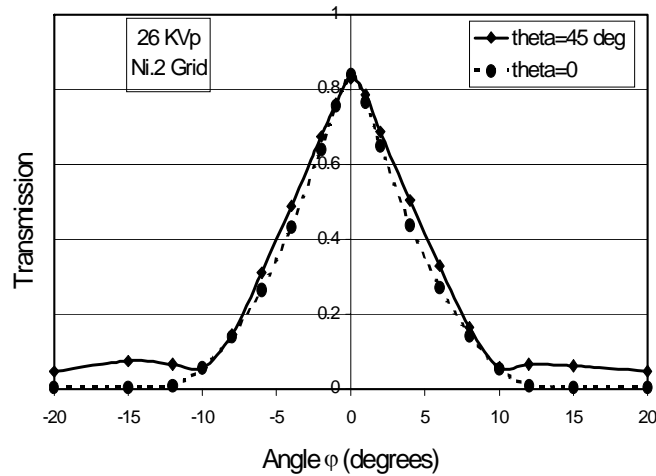


Fig. 11 Transmission of x-rays at 26 kVp for Ni.2 grid as a function of the normal incidence angle φ for $\theta = 0^\circ$ and $\theta = 45^\circ$.

4. SUMMARY OF EXPERIMENTAL RESULTS

The data shown in Figures 8-11 provide significant insight into the performance of a large focused grid. The transmission of primary radiation corresponds to the data taken at angle $\varphi = 0^\circ$. Reduction of the scattered radiation is dependent on the reduction of the transmission at angles $\varphi > 1^\circ$. The data indicate that 2D grids made of Ni with 20 μm lamella thickness, 300 μm period, and a grid height of 1.78 mm to 2.00 mm exhibit reduced transmission of scattered radiation ($\varphi > 1^\circ$) and increased transmission of primary radiation ($\varphi = 0^\circ$) compared to the conventional reference grid. Thus these 2D grids would have the benefit of producing a smaller scatter-to-primary ratio than a conventional reference grid, and improving contrast.

ACKNOWLEDGMENTS

The work was supported by NIH Grant: 1 R43 CA76752-01.

REFERENCES

1. D. R. Dance, J. Persliden and G. A. Carlsson, "Calculation of dose and contrast for two mammographic grids," *Phys. Med. Biol.***37**, 235-248 (1992).
2. A. J. Wagner, "Contrast and Grid Performance in Mammography," *Screen Film Mammography – Imaging Considerations and Medical Physics Responsibilities, Proc. Of the SEAAPM Spring Symposium*, April 6, 1990, Columbia, South Carolina, Gary T. Barnes and G. Donald Frey eds., Medical Physics Publishing, Madison, Wisconsin 1991, pp. 115-134.
3. R. Fahrig, J. Mainprize, N. Robert, A. Rogers and MJ Yaffe, "Performance of Glass Fiber Antiscatter Devices at Mammographic Energies", *Med. Phys.* **21**, 1277 (1994).
4. H. Bernstein, E. P. Muntz, J. Schreckendgust, D. J. Klein, and K. Lee, "A detailed experimental and theoretical comparison of the angular and energy dependencies of grid transmission," *Med. Phys.* **10**, Mar/Apr, 216-223 (1983).
5. H. Bernstein and E. P. Muntz, "Experimental verification of a technique for predicting scattered radiation transfer: Application to low photon energies," *Med. Phys.* **13**, Nov/Dec, 836-842 (1986).
6. D. P. Chakraborty, "Effect of the Anti-Scatter Grid and Target/Filters in Full-Field digital mammography," *Physics of Medical Imaging*, SPIE 3659, 878-885 (1999).
7. D.R. Dance and G.J. Day, "The computation of scatter in mammography by Monte Carlo methods," *Phys. Med. Biol.* **29**(3), 237-247 (1984).
8. "International Standard Diagnostic X-ray imaging equipment – Characteristics of mammographic anti-scatter grids", International Electrotechnical Commission Publication 61953, 1997.
9. D. J. Klein, E. P. Muntz, K. Doi, K. Lee, P. Chopelas, H. Bernstein, and J. Lee, "Experimental and theoretical energy and angular dependencies of scattered radiation in the mammography energy range," *Med. Phys.* **10**, Sep/Oct, 664-668 (1983).
10. Z. Lin, L. F. Plut and V. N. Cooper, "Grids and Digital Grids: Improvement of Contrast and SNR in Digital Radiography," *Physics of Medical Imaging*, SPIE 3659, 594-602 (1999).
11. E. P. Muntz, T. Fewell, R. Jennings, and H. Bernstein, " On the Significance of Very Small Angle Scattered Radiation to Radiographic Imaging at Low Energies", *Med. Phys.* **10**, 819 (1983).
12. M. J. Yaffe, R. E Hendrick, S. A. Feig, L. N. Rothenberg, J. Och and R. Gagne, "Recommended Specifications for New Mammography Equipment: Report of the ACR-CDC Focus Group on Mammography Equipment," *Radiology* **197**, 19-26 (1995).
13. H. Guckel, K. J. Skrobis, J. Klein, and T. R. Christenson, "Micromechanics via X-Ray Assisted Processing," *J. Vac. Sci. Technol. A* **12**, 2559 (1994).
14. E. W. Becker, W. Ehrfeld, P. Haggmann, A. Maner and D. Munchmeyer, "Fabrication of Microstructures with high aspect ratios and great structural heights by synchrotron

- Radiation Lithography, Galvanofforming, and Plastic Molding (LIGA Process),” *Microelectron. Eng.* **4**, 35 (1986).
15. C. M. Tang, E. Stier, K. Fischer and H. Guckel, “Anti-scattering X-ray Grids,” *Microsystem Technologies* **4**, pp. 187-192 (1998).
 16. C. M. Tang, K. Fischer, B. Chadhuri, H. Guckel, T. Fewell, R. J. Jennings, R. Fahrig, D. Jaffray, and M. Yaffe, “Precision fabrication of two-dimensional anti-scatter grids,” Submitted to SPIE International symposium Medical Imaging 2000, San Diego, CA, 12-17 February 2000.
 17. G.T. Barnes and I.A. Brezovich, “The intensity of scattered radiation in mammography,” *Radiology* **126**, 243-247 (1978).
 18. Z. Jing, W. Huda, and J.K. Walker, “Scattered radiation in scanning slot mammography,” *Med. Phys.* **25**, 1111-1117 (1998).
 19. T.R. Fewell and R.E. Shuping, *Handbook of Mammographic X-ray Spectra*, DHEW Publ. (FDA) 79-8071 (U.S. GPO, Washington, DC, 1978).
 20. W.R. Nelson, H. Hirayama, and D.W.O. Rogers, “The EGS4 code system,” SLAC-Report-265, Stanford Linear Accelerator Center, 1985.
 21. Y. Namito, S. Ban, and H. Hirayama, “LSCAT: Low-energy photon-scattering expansion for the EGS4 code,” KEK Internal 95-10, National Laboratory For High Energy Physics, Japan, 1995.
 22. C. J. Leliveld, J.G. Mass, V.R. Bom, and C.W.E. van Eijk, “Monte Carlo modeling of coherent scattering: Influence or interference,” *IEEE Trans. Nucl. Sci.* **43**, 3315-3321 (1996).